

Elemental quantification using multiple-energy x-ray absorptiometry

N Kozul, G R Davis, P Anderson and J C Elliott

Department of Biophysics in Relation to Dentistry, St Bartholomew's and the Royal London School of Medicine and Dentistry, Queen Mary and Westfield College, Mile End Road, London E1 4NS, UK

Received 6 November 1998, in final form and accepted for publication 22 December 1998

Abstract. A novel implementation of multiple-energy x-ray absorptiometry (MEXA) for elemental quantification has been developed. Species are resolved on the basis of their differential attenuation spectra across a wide energy range, ideally including absorption edges. By measuring the incident and exiting x-ray spectra and using known values of mass attenuation coefficients over selected energy bands, the density line integral of the species along the x-ray path can be calculated from all the selected energy channels simultaneously by non-linear least squares methods. Effects of 'escape' peak phenomena are modelled and corrections for them are included in the MEXA software. The applications of MEXA are illustrated by single measurements on aluminium and zirconium foils, quantitation of aqueous KI diffusing into a porous solid, simultaneous measurement of acidic diffusant (CH_3ICOOH) and porous solid with which it reacts and which it dissolves and microtomographic reconstructions of liquid and solid specimens containing caesium and/or iodine.

Keywords: x-ray instrumentation, chemical analyses, ionic diffusion in liquids, x-ray tomography

1. Introduction

Electron-probe microanalysis and particle-induced x-ray emission are standard methods for quantitative elemental analysis on a microscopic scale. However, these techniques require a vacuum and are therefore not applicable to systems containing liquids. Furthermore, these techniques are limited to surface layers a few micrometres thick because the depths to which electrons and other particles penetrate are limited. Some of these drawbacks can be overcome by the use of x-ray fluorescence microprobes which can be used to give information within the depth of a specimen, including liquids. However, a synchrotron source is required because of the low yield of fluorescence x-rays and quantitation is difficult, particularly for heterogeneous specimens, because corrections for absorption of the primary and secondary x-rays are required. For these reasons, many experiments that require elemental discrimination on a microscopic scale are difficult or impossible to undertake. Examples include the diffusion, flow and reaction of species in liquids held within porous solids and changes in distribution of species in solids as a result of mechanical deformation. To overcome these existing limitations, we have developed and investigated the application of multiple-energy x-ray absorptiometry (MEXA) on a microscopic scale. MEXA is essentially a generalized form of dual-energy x-ray absorptiometry (DEXA), which is used in medical diagnosis for the determination of bone density independently of soft

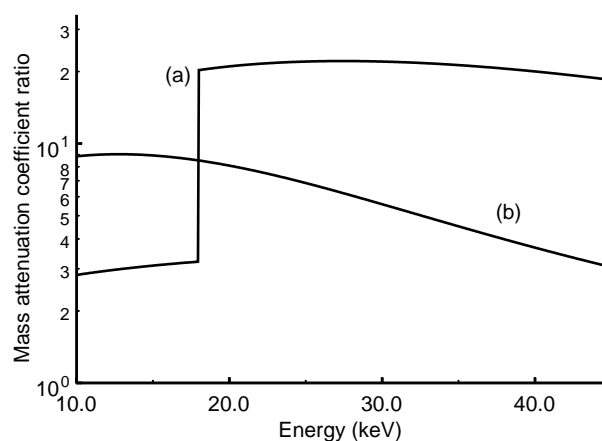


Figure 1. Changes in the ratios of mass attenuation coefficient with energy for (a) Zr and Al and (b) HAP and H_2O .

tissue. Such measurements can give the integral of the concentration of species along a linear path through the depth of a specimen. The ratio of x-ray attenuation coefficients of any two elements changes with x-ray energy (figure 1), the greatest changes occurring at absorption edges (a). At higher energies, in the absence of absorption edges, more gradual changes due to various mechanisms of attenuation occur (b). Species differentiation is still possible when absorption edges are at inaccessible energies, but a wider energy range is required. The rate of change in ratio with energy tends to increase with increasing difference in atomic number.

† E-mail address: g.r.davis@mds.qmw.ac.uk

Various experimental arrangements have been used for determining individual elemental (or species) concentrations from x-ray attenuation at various energies. These include the use of isotope sources [1], use of K-edge filters [2], changing x-ray acceleration voltage [2], changing x-ray target materials [3,4], use of crystal spectrometers [5], use of tuneable monochromatized synchrotron radiation [6] and use of energy-dispersive detectors [7, 8]. The main application of the first three of the above methods is to bone densitometry by using two attenuation measurements to calculate the masses of hard and soft body tissue or, when no hard tissue is present in the path, lean and fat tissue [2]. Typical energies are 70–140 keV. These methods rely on gradual changes in x-ray attenuation ratios because biological tissues do not contain in detectable amounts elements with absorption edges in the useable energy range. The use of three energies from radio-isotope sources to distinguish bone, lean and fat tissue has been reported by Jonson *et al* [9], whereas an attempt to resolve four species (bone, collagen, lean tissue and fat), at three or four relatively low photon energies, was made by Kairento [10] and Kairento and Spring [11]. A method for quantifying three species (bone, soft tissue and fat), using a wide energy band in the x-ray spectrum [8, 12], has also been proposed.

The potential for resolving species by x-ray absorptiometry in materials and other non-medical fields has not been widely investigated. Cazaux [3] used a system with a fan-beam x-ray microtomography (XMT) scanner and a non-energy-dispersive CCD camera for elemental (species) mapping and for monitoring diffusion processes in liquids [4]. Measurements were made with characteristic x-rays of selectable elements, one per element to be measured, arranged on a moveable x-ray target. The analysis made use of absorption edges in the useable energy range, assuming the radiation to be monochromatic. Microtomography has also been used for studying metal matrix composites [7] using 4% energy bands above and below the zirconium K absorption edge to differentiate between aluminium and zirconia. In this work, the energy bands were treated as monochromatic for analytical purposes. The width of the energy bands was selected as a compromise between obtaining sufficient photon counts (for acceptable noise levels) and avoiding polychromatic artefacts.

We now describe a novel method for generalized MEXA, using an energy-dispersive detector and a multi-channel analyser (MCA), such that all the selected MCA channels from a large portion of the x-ray spectrum are used to determine the specimen composition. This technique involves mathematically resolving the transmitted spectrum into a product of the incident spectrum and one or more attenuation spectra related to the mass attenuation coefficients of the species. Since this method uses essentially the whole available spectrum, it improves the signal-to-noise ratio and therefore reduces polychromatic errors. When two or more species are present, separate density line integrals (projected masses) of each of the species are obtained. Because many MCA channels are simultaneously used to calculate only a few parameters, the system of equations is overdetermined and is solved numerically using the non-linear least squares method (NLLSQ).

Significant errors in quantification can occur when a proportion of high-energy x-ray photons penetrating the specimen is recorded at a lower region in the spectrum due to fluorescent radiation escaping from the detector. The MEXA software includes an algorithm to correct for this 'escape-peak' phenomenon.

In this paper, we demonstrate the accuracy of MEXA, using single measurements of solid specimens (metal sheets) and XMT measurements of solid (Al rod) and liquid (aqueous solutions of KI and CsI) specimens, and the application of MEXA in diffusion and diffusion/reaction studies.

2. The theoretical background

For the purpose of this analysis, a specimen is considered to be constituted of r known species (elements or compounds) in unknown amounts. In an ideal system, when an x-ray beam passes through a specimen, x-rays are attenuated according to Beer's law:

$$I(E) = I_0(E) \exp \left(- \int_{(t)} \mu(s, E) ds \right) \quad (1)$$

where the exponent in the above equation is a line integral over the path length t through the specimen of the x-ray beam. At energy E , $I_0(E)$ is the intensity of incident radiation expressed as a count rate, $I(E)$ is the intensity of the exiting radiation and $\mu(s, E)$ is the linear attenuation coefficient (LAC) at a position s , the distance along the path through the specimen. In applying equation (1), it is assumed that the measured value of $I(E)$ is the true exiting count rate, i.e. no scattered radiation is detected, and that it is independent of the intensity of radiation in other parts of the spectrum.

Because species essentially absorb x-rays independently, a species mass attenuation coefficient (MAC) $\mu_m(E)$ can be defined by

$$\mu_m(E) = \mu(s, E) / \rho(s) \quad (2)$$

where $\rho(s)$ is the mass of the species per unit volume. Now (1) can be written as

$$I(E) = I_0(E) \exp \left(- \mu_m(E) \int_{(t)} \rho(s) ds \right) \quad (3)$$

in which we define the density line integral p by:

$$p = - \int_{(t)} \rho(s) ds. \quad (4)$$

For a specimen consisting of r species, equation (3) becomes

$$I(E) = I_0(E) \exp \left(- \sum_{k=1}^r \mu_{mk}(E) p_k \right). \quad (5)$$

With an x-ray spectrum sampled at discrete energies E_i , where $i = 1, \dots, n$, equation (5) gives the set of n simultaneous equations

$$\frac{I(E_i)}{I_0(E_i)} = \exp \left(- \sum_{k=1}^r \mu_{mk}(E_i) p_k \right). \quad (6)$$

The terms on the left-hand side can be determined experimentally and μ_{mk} can be calculated from published

data of elemental MACs [13–15]. If $i < k$, p_k cannot be determined uniquely from equation (6); if $i = k$, p_k can be determined; and if $i > k$, p_k is overdetermined. In the latter case, which is the situation here, p_k can be estimated from the condition of the best fit, in a least squares sense, between the observed and the calculated values of $I(E_i)/I_0(E_i)$.

Because the calculated values are not linear functions of the parameters, NLLSQ must be used, though an approximate solution can be determined using linear methods (see later). The accuracy with which the concentrations of individual species can be resolved from others depends on the relative variability of their MACs over the energy range used and on the photon-counting statistics.

2.1. Software implementation

The analysis software was written in the C++ programming language. The input data required are as follows.

- (i) The exit spectrum $I(E)$, recorded over the useable energy range as photon counts in each energy channel with a record of the time when the measurement was taken, plus the real and live times (the live time is the real time minus the dead time).
- (ii) The incident spectrum $I_0(E)$, recorded at known times before and after the exit spectrum recordings.
- (iii) An experimentally determined ‘look-up’ table of energy-calibration points (channel number versus energy) for known absorption edges and target emission lines, or separately measured calibration energies.
- (iv) A ‘look-up’ table of the MACs for all the species over the energy range used derived from published elemental values [13–15].

2.1.1. The calibration of channels in terms of energy. A linear calibration function is determined by weighted linear least squares (LLSQ). The points from the calibration ‘look-up’ table that are used and their weights are user selectable, so that the straight line can be forced through (or close to) strategic points. For example, in a study involving zirconium, a point corresponding to the zirconium absorption edge would be given a high weight. There was no evidence of departure from a straight line.

2.1.2. Standardization of incident intensities. To correct for slow changes in the incident intensity, $I_0(E)$ standards are taken before and after sets of $I(E)$ measurements and estimated values for $I_0(E)$ for each $I(E)$ are determined by linear interpolation using the times of data collection. No further analytical corrections for dead time or pile-up were made (compensation is incorporated into the counting system).

2.1.3. Correction for escape peaks. Correction for escape peaks is performed by subtracting a running ‘escape spectrum’ from the experimental one, starting at an energy equal to the accelerating potential minus the fluorescence energy and working towards lower energies. The ‘escape spectrum’ is determined using the calibration function $r_i = f(E_i)$ (where r_i is the ratio of ‘escape’ to main peak areas and E_i is the energy of the main peak).

2.1.4. Determination of approximate solutions by LLSQ.

Values of p_k are derived by LLSQ fitting of the linearized form of equation (6):

$$\log \left(\frac{I_0(E_i)}{I(E_i)} \right) = \sum_{k=1}^r \mu_{mk}(E_i) p_k. \quad (7)$$

This provides a close first estimate of the parameters for the NLLSQ process, thus avoiding false minima and reducing the number of iterations required. The LLSQ results are biased because the uncertainty (noise) in a calculated density line integral is not linearly related to the noise in the intensity measurements because

$$\log(I(E) + \delta I(E)) \neq \log I(E) + a \delta I(E) \quad (8)$$

where δI is the noise and a is a constant.

2.1.5. The NLLSQ procedure. The weights used in the NLLSQ calculations are $1/\sigma^2$, where

$$\sigma^2 = \left(\frac{N(E)}{N_0(E)} \right)^2 \left(\frac{T_0}{T} \right)^2 \left(\frac{1}{N_0(E)} + \frac{1}{N(E)} \right) \quad (9)$$

and $N_0(E)$ and $N(E)$ are photon counts (prior to correction for escape peaks) collected during the live times T_0 and T used for determining $I_0(E)$ and $I(E)$ respectively. This system of weighting takes into account errors both in $N_0(E)$ and in $N(E)$ whilst treating them as uncorrelated. The system of normal equations derived from equation (6) is solved using Gaussian elimination. Refinements are continued until the difference between the parameter values for consecutive cycles is less than 0.01%.

2.1.6. Software output. The density line integrals are output together with a measure of the quality of fit, given by

$$R^2 = 100 \sum_{i=1}^m (I(E_i)_{calc} - I(E_i)_{exp})^2 / I(E_i)_{calc}^2 \quad (10)$$

for every cycle. The variance–covariance matrix was calculated at the end as the inverse of the normal equations matrix, which had been formed as a part of the NLLSQ parameter calculation.

2.1.7. The performance of the software. Normally, up to ten cycles were required for convergence. The validity of the software was checked by using simulated data sets (generated from ideal spectra, with random Gaussian noise added to each point). The variances from the variance–covariance matrix for individual simulated data sets were compared with variances calculated directly from the line integrals deduced from a large number (200–500) of simulated data sets. The calculated line integrals agreed with the models used for the simulation and the variances from the variance–covariance matrix agreed with directly calculated variances to within $\pm 10\%$.

3. Experimental details

3.1. Apparatus

A Hilger & Watts Y33 microfocuss x-ray generator was used with either a tungsten or a silver target. The beam was collimated using crossed tantalum slits (each about 15 μm wide) placed 30 mm from the source. Spectra were recorded using a planar high-purity germanium (HPGe) detector (active diameter 6 mm, detector-to-specimen distance 30 cm), using a 672 Spectroscopy Amplifier set for Gaussian pulse shaping (0.5 μs shaping time) and a 921 MCA with 2048 channels and a conversion time of 1.25 μs (all EG&G, Oak Ridge, USA). Up to 0.25 s could be taken for reading and storing each spectrum. Pile-up rejection and corrections for dead time were incorporated into the amplifier–MCA system. The recorded spectra exhibited escape ‘peaks’ in the region of 10 keV below each element of the true spectrum, as a result of fluorescence photons escaping from the germanium ($K\alpha$ at 9.868 keV, $K\beta_1$ at 10.984 keV and $K\beta_2$ at 11.103 keV).

3.2. Specimens

3.2.1. Single-measurement specimens.

- (i) Aluminium and zirconium sheets. An Al sheet, 1.2 mm \times 50 mm \times 50 mm and 99.98% pure and a Zr foil 0.025 mm \times 100 mm \times 100 mm and 99.9% pure were used (both Advent, Suffolk, England; all nominal dimensions). Their thicknesses (assumed to be uniform) were determined by weighing a sheet (estimated error $\pm 10^{-3}$ g) and measuring its dimensions with sliding calipers (estimated error $\pm 10^{-2}$ mm).

3.2.2. Specimens used for microtomography.

- (i) Aluminium: one-species specimen. An aluminium rod, 99.999% pure (Aldrich, UK), original diameter 6.35 mm, was cut to about 20 mm length and filed to about 4.7 mm diameter.
- (ii) Potassium iodide solution: two-species specimen (KI and H_2O). A $1.000 \pm 0.001 \text{ mol l}^{-1}$ aqueous solution of KI was made by weighing $16.600 \pm 0.001 \text{ g}$ KI (AnalaR, BDH Chemicals Ltd, Poole, UK, 99.8% purity) into a 100 ml volumetric flask made up with de-ionized water. A microtomography specimen was made by filling a small polypropylene vial (maximum internal diameter 5 mm, volume 0.2 ml) with solution. There are significant differences between the MACs at the K absorption edge of I (table 1).
- (iii) Caesium iodide solution: three-species specimen (I, Cs and H_2O). A $1.000 \pm 0.001 \text{ mol l}^{-1}$ aqueous solution of CsI was prepared from $12.990 \pm 0.001 \text{ g}$ CsI (AnalaR, Aldrich, UK, 99.9% purity) made up to 50 ml with de-ionized water. In addition to the I edge at 33.18 keV, the Cs edge is at 35.98 keV. There are again significant differences between the MACs at the I and Cs edges (table 1).
- (iv) Iodoacetic acid. A 0.5 mol l^{-1} aqueous solution of CH_2ICOOH was prepared from $9.295 \pm 0.001 \text{ g}$ of CH_2ICOOH (Sigma Chemical Co, MO, USA) made to 100 ml as above.

Table 1. Fractional mass attenuation coefficients of various species (mass attenuation coefficients multiplied by species fractional weight) just below and above the absorption edges of I (33.17 keV) and Cs (35.98 keV).

Absorption edge	Fractional mass attenuation coefficient ($\text{cm}^2 \text{g}^{-1}$)		
	KI	H_2O	
I (lower)	0.83	0.27	
I (upper)	4.22	0.27	
	I	Cs	H_2O
I (lower)	0.68	0.79	0.25
I (upper)	3.78	0.79	0.25
Cs (lower)	3.08	0.63	0.23
Cs (upper)	3.08	3.38	0.23

3.3. Experimental procedures

3.3.1. Calibration. The following calibration points were used, as appropriate, in the channel number versus energy ‘look-up’ table: characteristic L lines of tungsten ($L\alpha_1 L_{III} MV$, 8.398 keV; $L_1 \beta_{II} M_{IV}$, 9.672 keV; and $L\gamma_1 L_{II} O_1$, 11.468 keV); K absorption edges (Zr, 17.99 keV; I, 33.18 keV; and Cs, 35.98 keV) and characteristic fluorescence K lines excited by americium in a sealed source (Cu, 8.04 keV; Rb, 13.38 and 15.11 keV; Mo, 17.45 and 19.78 keV; Ag, 22.11 and 24.9 keV; and Ba 32.07, 36.39 and 37.26 keV). The same K lines were used for determination of the escape-to-main peak ratio, using a long data collection time in order to obtain good statistical accuracy.

3.3.2. Single measurements. Two sets of attenuation measurements were made for single sheets of Al and Zr and for a single sheet of Al plus a single sheet of Zr. The x-ray generator with a W target was run with (i) an accelerating voltage of 23 kV (to avoid the influence of the Ge ‘escape peaks’) and a tube current of 0.5 mA and (ii) an accelerating voltage of 45 kV (to estimate the influence of ‘escape’ peaks on the results) and a tube current of 1 mA. The metal sheets were placed near the aperture, so that little scattered radiation would enter the detector. Intensities were determined from ten single measurements, each made by determining the live time (section 2.1) required in order to collect 10 000 photons within the specified energy range. This typically took, for the 23 kV setting with energy range 18.52–21.58 keV, 227 and 232 s for single sheets of Al and Zr respectively, measured separately, and 681 s for Al and Zr sheets together; for the 45 kV setting with energy range 23.58–24.63 keV, 19.9 and 20.4 s for single sheets of Al and Zr respectively, measured separately, and 40.8 s for Al and Zr sheets together.

The intensity was calculated from the total counts (in a given channel) divided by the total live time. I_0 was measured before and after I (this typically took 65 and 9.8 s respectively for the 23 and 45 kV settings).

3.3.3. Microtomography of homogeneous species of known compositions. A first-generation XMT system was used to collect data for a single microtomographic slice [16]. The x-ray generator was used with a W target, an accelerating voltage of 45 kV and a tube current of 1.5 mA (the Ge ‘escape’

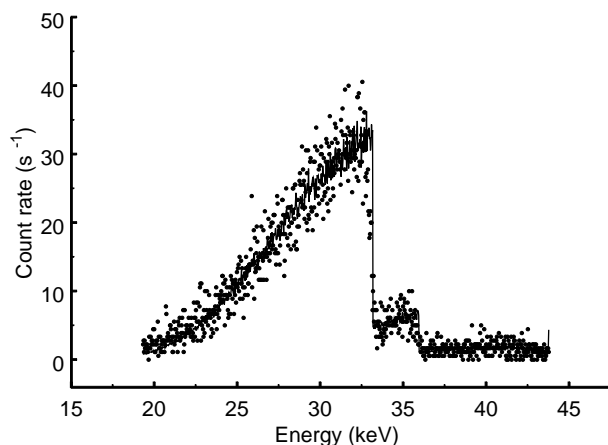


Figure 2. Experimental (dots) and modelled (line) exit spectra for aqueous CsI (1.0 mol l^{-1}) in a 5 mm diameter plastic phial (diametrical ray). The lower and upper absorption edges are due to I (33.17 keV) and Cs (35.98 keV) respectively. (X-ray tube with W target, 45 kV and 1.5 mA. Data collection time about 1.8 s, solution analysed for three species, namely Cs, I and H_2O .)

peaks would thus influence the detected spectrum at energies below 35 keV, but, because the x-ray photons have more energy, they penetrate further into the detector, thus reducing the probability of the escape of fluorescence radiation). For each projection, the specimen was stepped through the beam at 128 positions and an exit spectrum was recorded at each step; the specimen was then rotated by a small angle and the process was repeated so that 251 projections over 360° were measured (a typical data collection time was 48 h). The step sizes were $45 \mu\text{m}$ for Al rod and $52 \mu\text{m}$ for KI and CsI solutions. The intensity was measured by determining the live time required in order to collect a constant number of photons (typically 3000–5000) in 25.85–28.95 keV channels. Before and after every projection, standard spectra (I_0 measurements) were recorded, collecting five to eight times more counts than for the data files. Density line integrals for each species were determined for every data point and separate XMT images were computed for each of the species by using a back-projection algorithm.

3.3.4. Microtomography of the diffusion of KI into a rat femur and a human tooth root. A rat femur and a human tooth root were stored in aqueous KI solution (3 mol l^{-1}) for 19 and 10 days respectively at room temperature. First-generation XMT was used as before to obtain a single slice of each. An Ag target, an accelerating voltage of 45 kV and a tube current of 1.5 mA were used. For each of the 251 projections, the specimen was stepped past the beam and exit spectra were recorded at each of 128 steps $35 \mu\text{m}$ apart. The data were processed using two energy ranges, 27.28–31.60 and 35.06–37.36 keV (150 and 80 channels respectively) below and above the I absorption edge (33.17 keV). Two species were used, hydroxyapatite (HAP, $\text{Ca}_{10}(\text{PO}_4)_6(\text{OH})_2$), to model the mineral of the femur or tooth, and KI.

3.3.5. The diffusion cell. A 6.3 mm diameter hole was bored through a 9.4 mm thick $25 \text{ mm} \times 25 \text{ mm}$ block of

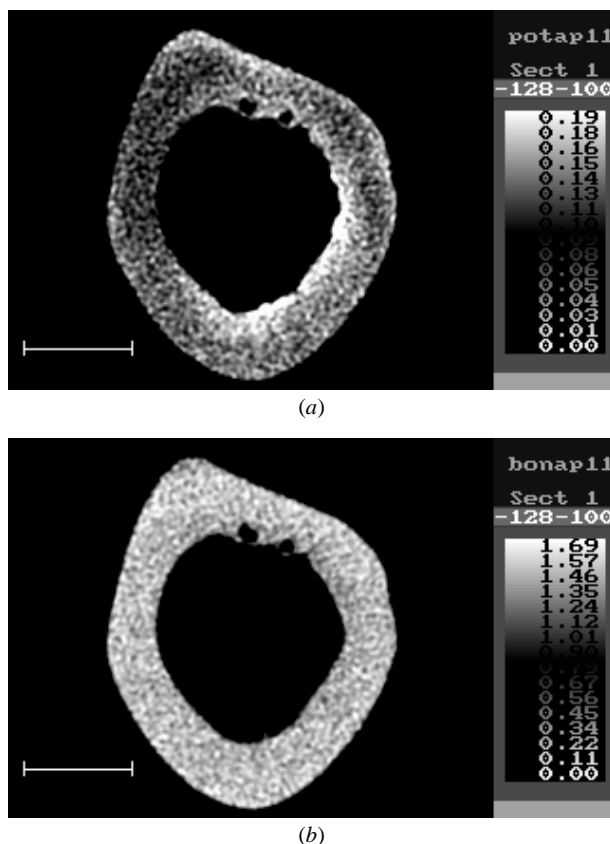


Figure 3. Microtomographic concentration maps (g cm^{-3}) of KI (a) and HAP (b) following diffusion of aqueous KI (3.0 mol l^{-1}) through a surface of a rat femur for 19 days. Scale bar 1 mm.

poly(methyl methacrylate) (PMMA). One end of the hole was sealed with a thin PMMA sheet. The hole was partially filled with chemically prepared HAP powder which was compressed to a length of 6.7 mm. The average porosity calculated from the mass was 38 vol%. The other end of the hole was then sealed with another PMMA sheet. Two 0.5 mm diameter holes were drilled into the PMMA block so that solutions could be pumped over the surface of the HAP powder. For several days prior to the start of the experiment, water was pumped through the cell at 4.2 ml min^{-1} . The diffusion cell was then mounted on the x-ray set (W target, 45 kV, 1.5 mA) so that the beam passed along the central axis of the cell and the integrated masses in the direction of diffusion were measured. Exit spectra with counting times of 30 s were recorded at 144 s intervals. After 3.5 h, the water flowing through the cell was replaced by 1.0 mol l^{-1} KI solution and exit spectra were recorded for a further 30 h. The MEXA software was used to determine the integrated masses per unit area (density line integrals) of KI and HAP along the cell axis throughout the period using the energy ranges 29.21–32.26 and 35.31–36.84 with KI and HAP plus estimated water (within the pores) for the two species. The KI solution was then replaced by water for several days to allow the KI to diffuse out, after which 0.5 mol l^{-1} aqueous CH_2ICOOH was made to flow through for a period of 90 h and exit spectra were recorded at 180 s intervals. MEXA was used

Table 2. Thicknesses of sheet specimens derived using MEXA.

Accelerating potential (kV)	Specimen ^a	Model	Escape-peak correction	Derived thickness (μm)	Standard deviation (μm)	Difference (%)
23	Al	Al	No	1175	9	-1.1
			Yes	1175	9	-1.0
		Al	No	1166	13	-1.8
			Yes	1166	18	-1.8
	Zr	Zr	No	0.4	0.9	
			Yes	0.4	0.9	
		Zr	No	22.6	0.5	-2.4
			Yes	22.6	0.5	-2.4
		Al	No	10	9	
			Yes	10	9	
		Zr	No	23.3	0.7	+0.9
			Yes	23.3	0.7	+0.8
	Al+Zr	Al	No	1171	13	-1.4
			Yes	1172	13	-1.3
		Zr	No	23.7	0.9	+2.6
			Yes	23.7	0.9	+2.4
45	Al	Al	No	1160	1	-2.3
			Yes	1195	1	-0.7
		Al	No	941	2	+23.1
			Yes	1187	3	0.0
		Zr	No	0.69	0.06	
			Yes	0.10	0.06	
	Zr	Zr	No	22.92	0.05	-0.8
			Yes	23.25	0.05	+0.7
		Al	No	23	1	
			Yes	10	1	
		Zr	No	23.30	0.04	-3.6
			Yes	23.90	0.04	+3.5
	Al+Zr	Al	No	1103	2	-14.5
			Yes	1171	3	-1.4
		Zr	No	26.20	0.07	+12.4
			Yes	22.90	0.01	-0.7

^a The measured thicknesses were 1187 and 23.1 μm for Al and Zr respectively.

to measure the integrated masses per unit area of CH_2ICOOH and HAP along the cell axis throughout the period, using the same energy ranges as before. All experiments were carried out at room temperature.

4. Results

4.1. Single-measurement specimens (Aluminium and zirconium sheets)

The energy ranges below and above the Zr absorption edge at 17.99 keV used for NLLSQ fitting were 13.04–17.61 and 19.13–21.58 keV (corresponding to 150 and 80 channels respectively) for the 23 kV accelerating potential and 13.04–17.61 and 19.13–30.73 keV (corresponding to 150 and 380 channels respectively) for the 45 kV accelerating potential. The results are given in table 2, in which the thicknesses were calculated from the density line integrals and the published densities. For the single-foil measurements, thicknesses were calculated with and without the other foil in the model. Results are presented with and without correction for escape peaks.

4.2. Specimens used for microtomography

The results for the 1.0 mol l^{-1} and solutions of KI and CsI (I and Cs edges at 33.17 and 35.98 keV respectively) are given in table 3, together with the energy ranges used. The presence of polypropylene was ignored in the analysis.

4.3. The diffusion of KI into a rat femur and a human tooth root

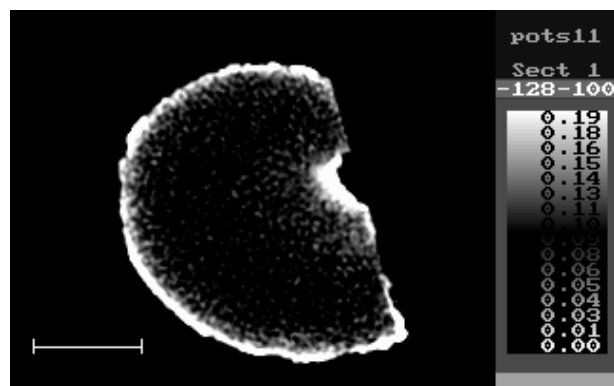
Microtomographic concentration maps of KI and HAP are given for a rat femur after immersion in 3.0 mol l^{-1} KI for 19 days (figure 3) and a human tooth root after immersion in 3.0 mol l^{-1} KI for 10 days (figure 4). The experimental and modelled spectra for one projection point are shown in figure 2.

4.4. Diffusion within porous media

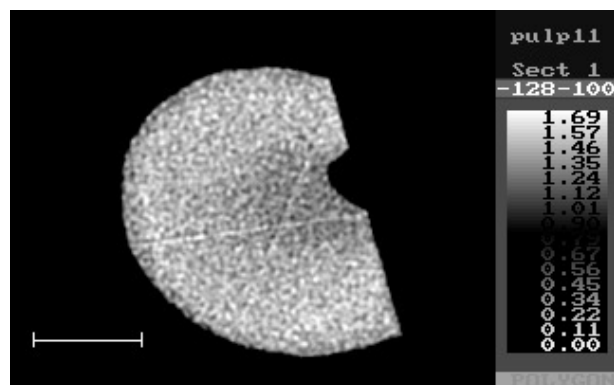
Figure 5 shows the integrated masses per unit area of KI within the pores and HAP during the diffusion of KI into the compressed HAP powder. Assuming that all the available pores within the HAP were filled with 1.0 mol l^{-1} KI, the final integrated mass per unit area of KI would be 0.045 g cm^{-2} . This is close to the limit value in figure 5, which suggests

Table 3. Results for microtomography specimens.

Specimen	Energy ^a range(s) (keV)	Species concentration (from composition) (g cm ⁻³)	Species concentration (experimental) (g cm ⁻³)	Difference (%)
Al	25.58–37.97	Al 2.698	2.699	+0.037
KI + H ₂ O	27.72–32.08	H ₂ O 0.947 ^b	1.003	+5.85
	34.45–39.96	KI 3.13	3.133	+0.096
CsI + H ₂ O	24.03–30.19	H ₂ O 0.942 ^b	1.1	+15.4
	34.09–34.99	I 4.93	5.165	+4.65
	37.35–39.49	Cs 1.873	1.859	−0.75

^a 100 channels \equiv 3.1 keV.^b Estimated from the reduction in mass of H₂O in 1 mol l⁻¹ KI solution (0.0533 cm³) or 1 mol l⁻¹ CsI solution (0.0576 cm³) assuming that the salt occupies the same volume as it does in the solid.

(a)

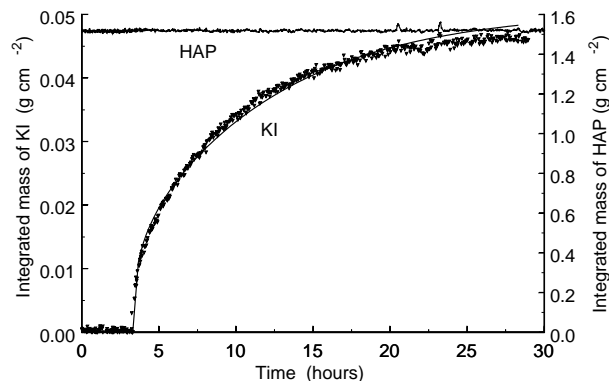
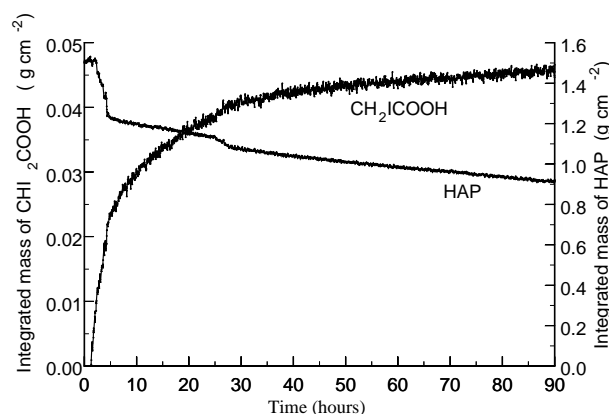


(b)

Figure 4. Microtomographic concentration maps (g cm⁻³) of KI (a) and HAP (b) following diffusion of aqueous KI (3.0 mol l⁻¹) through a surface of a root of a human tooth for 10 days. Scale bar is 1 mm.

that all the available pores were filled after 30 h. Also shown (full line) is the theoretical increase in the integrated mass per unit area of KI corrected for the porosity of the HAP calculated using the published bulk diffusion coefficient for KI in water of 2.0×10^{-5} cm² s⁻¹ [17]. This result shows that the tortuosity of the pores in the HAP has rather little effect on the diffusion of KI.

Figure 6 shows the decrease in integrated mass per unit area of HAP resulting from dissolution and the simultaneous increase in the mass per unit area of CH₂ICOOH due to

**Figure 5.** Integrated masses per unit area of HAP and KI as functions of time during diffusion of 1.0 mol l⁻¹ KI into compressed (38 vol% porosity) HAP. The full line shows the theoretical increase in integrated mass per unit area of KI.**Figure 6.** Integrated masses per unit area of HAP and CH₂ICOOH as functions of time during diffusion of 0.5 mol l⁻¹ CH₂ICOOH into HAP, compressed initially to 38 vol% porosity, showing the decrease in integrated mass per unit area of HAP as dissolution in acid occurs.

its diffusion inwards. Assuming that all available pores within the HAP at the start were filled with 0.5 mol l⁻¹ CH₂ICOOH, the mass per unit area of CH₂ICOOH would be 0.0249 g cm⁻². However, the mass per unit area at the end of the experiment is 0.046 g cm⁻², showing that there was an increase in porosity due to dissolution of HAP.

5. Discussion and conclusions

The results show clearly that MEXA can give, in suitable circumstances, accurate measurements of density line integrals for individual species in multi-species samples. It is noticeable that percentage errors are often larger than would be expected purely from photon statistics alone (variance-covariance), indicating the presence of systematic errors. As is to be expected, the error in the determination of water (table 3) is much larger than those for other species due to its fractional mass attenuation coefficient being much lower (table 1).

The energy ranges used for analysis of single measurements of Al and Zr sheets were below and above the Zr absorption edge at 17.99 keV. When a 45 kV accelerating potential was used, the analysis was seriously affected by the escape-peak phenomenon (affecting the spectrum below 35 keV). However, when correction for escape peaks was included in the processing of experimental spectra collected with a 45 kV accelerating potential, a significant improvement in accuracy was observed (the maximum error in the experimentally measured Al sheet thickness was reduced in magnitude from -14.5 to $+1.40\%$). In order to avoid escape-peak errors altogether, the foil experiment was performed with an accelerating voltage of 23 kV, using only energies above 13 keV in the analysis. This resulted in a great increase in acquisition time, due to the reduction in x-ray intensity. As can be seen in table 2, there is now virtually no difference between the results with and without correction for escape peaks.

With the inclusion of correction for escape peaks, it is clearly possible to obtain very accurate results, assuming that accurate mass attenuation coefficients are used. It is clear from table 2 that random errors in the experiments reported here are very small, but they will be important for the observation of small changes in the density line integral. Random errors are primarily due to photon-counting statistics and can be reduced by using longer counting times and by optimizing the incident spectrum to obtain the best species resolution. This optimization will be aided by mathematical modelling of the statistical uncertainty of the resulting species density line integrals as a function of photon counts over the detected spectrum. On the other hand, the systematic errors in table 2 are clearly quite large. These errors mostly arise from non-linearities in the counting system, particularly due to unresolved pulse pile-up and the influence of the detected intensity on the measured photon energy. These sources of systematic error need to be investigated further and integrated into the attenuation model.

The study of the diffusion of solutes within porous media is important in many chemical engineering disciplines (reviewed by Adler [18]). The tortuosity or connectivity of the pores, as well as the porosity, can have significant effects on the diffusion process. As a development of x-ray attenuation methods to measure local solute concentrations within porous solids [19], MEXA can be used to simultaneously determine the amounts of porous solid

and diffusing solute. This will be particularly useful in diffusion-reaction systems in which the amount of porous solid is also changing, for example, when the solid is dissolving during inward diffusion of acid.

In conclusion, we have demonstrated that MEXA can be used with laboratory sources to give accurate density line integrals of appropriate species over areas of $15\ \mu\text{m} \times 15\ \mu\text{m}$ through specimens 1 mm or more thick. MEXA has the advantage over existing micromethods that a vacuum is not required and a longer sampling length is possible. This will allow one to perform a range of hitherto impossible experiments involving quantitation of diffusion, flow and reaction in liquids within porous solids.

Acknowledgments

This work was supported by the Engineering and Physical Science Research Council (grant GR/J255628) and, latterly, by the Medical Research Council (grant G9505593MA).

References

- [1] Ryan P J and Fogelman I 1995 *Seminars Nucl. Med.* **26** 76–91
- [2] Laskey M A 1996 *Nutrition* **12** 45–51
- [3] Cazaux J 1993 *Microsc. Microanal. Microstruct.* **4** 513–37
- [4] Rondot S, Cazaux J, Aaboubi O, Chopart J P and Oliver A 1994 *Science* **263** 1739–41
- [5] Cosslett V E and Nixon W C 1960 *X-ray Microscopy* (Cambridge: Cambridge University Press) p 156
- [6] Bonse U, Nusshardt R, Busch F, Pahl R, Johnson Q, Kinney J, Saroyan R and Nichols M 1989 *Rev. Sci. Instrum.* **60** 2478–81
- [7] Justice I, Anderson P, Davis G R, Derby B and Elliott J C 1996 *Proc. 7th European Conf. on Composite Materials* (London: Woodhead) p 407
- [8] Jonson R, Roos B and Hansson T 1986 *Acta Radiologica: Diagnosis* **27** 105–9
- [9] Jonson R, Roos B and Hansson T 1988 *Acta Radiol.* **29** 461–4
- [10] Kairento A-L 1974 *Phys. Fennica* **9** 67–75
- [11] Kairento A-L and Spring E 1974 *Am. Ann. Clin. Res.* **6** 80–5
- [12] Kotzki P O, Mariano-Goulart D and Rossi M 1991 *Phys. Med. Biol.* **36** 429–37
- [13] Saloman E B, Hubbell J H and Schofield J H 1988 *Atom. Data Nucl. Data Tables* **38** 1–197
- [14] Hubbell J H and Seltzer S M 1995 *Tables of X-ray Mass Attenuation Coefficients and Mass Energy-Absorption Coefficients 1 keV to 20 MeV for Elements Z = 1 to 92 and 48 Additional Substances of Dosimetric Interest* (Gaithersburg: National Institute of Standards and Technology) report NISTIR 5632
- [15] Berger M J and Hubbell J H 1987 *XCOM: Photon Cross sections on a Personal Computer* (Gaithersburg: National Bureau of Standards) internal report NBSIR 87-3597
- [16] Elliott J C, Anderson P, Davis G R, Wong F S L and Dover S D 1994 *JOM—J. Miner. Mater. Soc.* **46** 11–19
- [17] Lide D R *et al* (ed) 1994 *CRC Handbook of Chemistry and Physics* (Boca Raton, FL: CRC) p 590
- [18] Adler P M 1992 *Porous Media: Geometry and Transports* (Stoneham: Butterworth-Heinemann) p 2
- [19] Dowker S E P, Anderson P and Elliott J C 1996 *Microsc. Microanal. Microstruct.* **7** 49–63